

On the three-dimensional precessing jet flow past a sudden expansion

Gioacchino Cafiero · Giuseppe Ceglia ·
Stefano Discetti · Andrea Ianiro · Tommaso Astarita ·
Gennaro Cardone

Received: 7 June 2013 / Revised: 20 January 2014 / Accepted: 22 January 2014 / Published online: 4 February 2014
© Springer-Verlag Berlin Heidelberg 2014

Abstract A circular jet flow past an abrupt expansion under some conditions switches intermittently between two states: quasi-axisymmetric expansion and gyroscopic-like precessing motion. In this work, an experimental investigation into the self-excited precessing flow generated by a 5:1 expansion of a round jet in a coaxial cylindrical chamber is carried out by means of tomographic particle image velocimetry. The experiments are performed on a jet issued from a short pipe at a Reynolds number equal to 150,000. Proper orthogonal decomposition (POD) is applied to extract information on the organization of the large coherent structures of the precessing motion. The application of this technique highlights the dominance of three modes: the most energetic two are associated with the jet precession; the third one is representative of the axial motion. An estimate of the precession probability based on the modal energy obtained from the application of POD is proposed. The precession frequency is extracted using a low-order reconstruction (LOR) of a subset of the POD modes. The reconstructed flow field topology obtained by the LOR highlights an underlying mechanism of swirl

generation in proximity of the inlet nozzle; the phenomenon is closely related to the interaction between the entrainment in the far field and the recirculation regions in the near field. The application of a stability criterion shows that the self-induced swirl flow results to be unstable. The instability is responsible for the generation of helical-shaped vortices in the near field, even though the dominant feature for the unconfined jet issued from the same nozzle is the axisymmetric ring-vortices generation.

1 Introduction

Considerable attention has been devoted to the development of devices with the aim of exciting and enhancing the large-scale coherent structures embedded into the shear layer of turbulent jets. The organization of these energy-containing structures plays a key role in the transport of mass and momentum in flames (Broadwell and Mungal 1991). These devices can be bundled in three categories as a function of the excitation source: acoustic (see Reynolds et al. 2003 for a review), mechanical (Simmons et al. 1981) and fluidic (such as precessing jets, Nathan et al. 1998).

The precessing jet (PJ) is generated with an axisymmetric jet flowing through a circular nozzle and subject to an abrupt expansion into a cylindrical chamber (coaxial with the nozzle, but with larger diameter). Under certain conditions, the jet reattaches asymmetrically to the chamber wall after the abrupt expansion, while on the opposite side, external fluid is entrained into the chamber. The instantaneous asymmetry triggers a rotating pressure field, inducing a precession of the jet, i.e., a rotation of the jet axis around the nozzle-chamber one. The PJ has some analogies with swirl flows in which, for relatively strong

Electronic supplementary material The online version of this article (doi:10.1007/s00348-014-1677-9) contains supplementary material, which is available to authorized users.

G. Cafiero (✉) · G. Ceglia · T. Astarita · G. Cardone
Dipartimento di Ingegneria Industriale - Sezione Aerospazio,
Università degli Studi di Napoli Federico II, P.le Tecchio 80,
80125 Naples, Italy
e-mail: gioacchino.cafiero@unina.it

S. Discetti (✉) · A. Ianiro
Departamento de Bioingeniería e Ingeniería Aeroespacial,
Universidad Carlos III de Madrid, Av. de la Universidad 30,
28911 Leganés, Spain
e-mail: sdiscett@ing.uc3m.es

swirl, a precession around the jet axis has been widely documented (the so-called precessing vortex core; see Syred 2006 for a review).

The description of the phenomenology of the PJ is extensively provided by Nathan et al. (1998). The flow exhibits an intermittent behavior, switching between the precessing and the axial mode. In the former, the flow field is characterized by a continuously unstable reattaching jet with a strong recirculation region located on the opposite side of the chamber. A transverse pressure gradient in the outflow is established, thus determining a sharp deflection of the wall jet at the exit of the chamber. Since the flow is in a condition of neutral equilibrium, the effect of any asymmetry and/or the turbulence fluctuations induce the reattachment point to move; as the jet starts to rotate along one direction, the asymmetry of the flow entrained into the chamber induces the establishment of a rotating pressure field. Indeed, the recirculating fluid moves upstream within the chamber and swirls in the direction opposite to that of the precession, thus retaining the net angular momentum equal to zero.

The PJ has shown extremely interesting features in terms of reduction in the global flame strain, thus leading to an increase in the volume of soot and radiation heat transfer to the furnace (Stamatov and Stamatova 2006). The increased radiative heat transfer induces a reduction in the flame temperature and in the production of NO_x (Newbold et al. 2000; Nathan et al. 2006). PJs have found application in industrial processes in which the radiant heat transfer plays a leading role over convection, such as rotary kilns for the production of cement and lime.

The parameters that characterize the flow field features of a PJ are: the thermodynamics properties (density ρ , dynamic viscosity μ), the jet velocity V_j , the jet precession frequency f_p , the nozzle diameter d , the external chamber diameter D and length L . According to the Buckingham-Pi theorem (Buckingham 1914), the following four non-dimensional groups can be addressed as governing parameters: $\text{St}_d, \text{Re}_d, \frac{D}{d}, \frac{L}{D}$, where:

$$\text{St}_d = \frac{f_p d}{V_j} \quad (1)$$

$$\text{Re}_d = \frac{\rho V_j d}{\mu}. \quad (2)$$

Several studies have concentrated their focus on identifying the best geometric and fluid dynamic conditions to favor jet precession. Nathan et al. (1998), together with many following works of the same research group (Newbold et al. 2000; Mi et al. 2001a; Nathan et al. 2006), focused the interest on the geometry optimization task. In most of the cited works, the expansion ratio is fixed to $D/d = 5$, which has shown to be very favorable for the

precession. Madej et al. (2011) have studied the effects of the chamber aspect ratio L/D and of the Reynolds number Re_d on the probability of precession, showing that it is a strong function of L/D (maximum in the range $2 < \frac{L}{D} < 2.75$, with a strong reduction at $L/D=3$) and a weakly increasing function of Re_d .

Measuring the Strouhal number associated with the precession St_d and its dependence on the geometric and flow parameters is of fundamental importance as it determines the intensity of mixing outside of the chamber. Mi and Nathan (2004, 2006) investigated the influence of the aspect ratio, the inlet geometry and the Reynolds number on St_d . They observed that it increases almost linearly with both the aspect ratio and Re_d .

Despite of all the previous research, the investigation of the instantaneous flow field topology is extremely challenging and it is not yet fully characterized, since it is strongly unsteady and three dimensional. Although PJs have already been used for several applications, there are many aspects that still require a deeper understanding to improve their performances; furthermore, PJs belong to the class of bifurcating flow instabilities arising in symmetrical configuration in absence of initial bias, which are usually difficult to be modeled and numerically simulated (Guo et al. 2001). Very limited attention has been dedicated in the past works on the topology of the flow field within the chamber. So far, these investigations have been performed with flow visualization (Nathan et al. 1998), phase-averaged measurements with pointwise techniques (Wong et al. 2004) or with numerical simulations (Guo et al. 2001, Revuelta et al. 2004). A clearer knowledge of the flow field instantaneous topology would further increase industrial interest in the device.

In this study, insight into the phenomenology of the fluidic PJs using tomographic particle image velocimetry (Tomo-PIV) (Scarano 2013) is provided. Tomo-PIV, in this sense, can provide a leap forward in understanding the organization of the flow topology in the complicate scenario of an unsteady, intermittent and strongly three-dimensional turbulent flow field; moreover, this technique is already well assessed for the study of jet flows (see e.g., Violato et al. 2012; Ceglia et al. 2014). The statistical features of the flow emerging from a fluidic PJ are presented. POD is herein used to extract relevant information about the coherent structures of the motion. A low-order reconstruction (LOR) approach (Ben Chiekh et al. 2004) is implemented to infer the precession frequency and the characteristic Strouhal number of the motion. This approach is expected to be more robust than measurement of pressure signals (see Nathan et al. 1998) or analysis of planar data (as in Madej et al. 2011); indeed, it accounts for the overall organization of the flow field. The instantaneous

flow field topology is described, providing an insight in the vortices generation and development. A stability criterion has been applied to characterize the self-induced swirling flow.

2 Experiment outline

2.1 Experimental apparatus

The jet is issued from a short-pipe nozzle (with diameter $d = 20$ mm and length $6.2d$, with a smooth contraction at its inlet) installed on the bottom of a nine-sided water tank facility (internal diameter 600 mm, height 700 mm). The jet expands with a step-like inflow condition into a cylindrical chamber coaxial with the nozzle (diameter $D = 100$ mm, length $L = 275$ mm, so that $D/d = 5$ and $L/D = 2.75$; see Fig. 1 for details on the nozzle geometry and on the reference frame). Both the tank and the cylindrical chamber are made of Plexiglas in order to ensure a full optical access. While in many investigations an exit lip (Nathan et al. 1992) and/or a centerbody (Wong et al. 2003) has been included into the chamber to favor the precessing motion and to condition the exit angle, in this study these arrangements are not considered in order to assess the topology of the flow field without external forcing.

A stabilized water mass flow rate of 2.3 kg/s is provided upstream of the nozzle by a centrifugal pump, and it is laminarized by passing through flow conditioning grids and honeycombs installed into the plenum chamber (with diameter and length equal to $5d$ and $20d$, respectively).

The flow is seeded with neutrally buoyant polyamide particles with an average diameter of $56 \mu\text{m}$, dispersed homogeneously within the facility with a concentration of approximately 0.15 particles/ mm^3 . Laser pulses are produced with a double-cavity Gemini PIV Nd:YAG laser system (532 nm, 200 mJ/pulse, 5-ns pulse duration). The

exit beam of 5 mm diameter is shaped into a parallelepiped volume. A knife-edged slit is placed along the laser path to obtain an YZ section of the illuminated volume of 250×34 mm. Four LaVision Imager sCMOS 5.5 megapixels cameras with identical lenses (100-mm focal length objectives) in Scheimpflug arrangement are placed on one side of the water facility, as sketched in Fig. 2. The lenses are set to $f_{\#} = 16$. The average magnification in the center of the measurement volume is about 0.06. This leads to a depth of field of more than 200 mm, a digital resolution of 10 pixels/mm and a particle diffraction limited minimum image diameter of 3.4 pixels (Adrian and Westerweel 2011).

The acquisition is performed directly in RAM memory on a workstation equipped with 96 GB of RAM memory. Sequences of the tracer particles with time separation of $130 \mu\text{s}$ are captured at a frequency equal to 10 Hz; the acquisition in RAM memory ensures that the probability of dropped frames is minimized. The 10 Hz frequency is not sufficient for the sampling of the temporal evolution of the vortical features within the shear layer. Nevertheless, it certainly suffices to temporally resolve the jet precession, which frequency is expected to be about 1 Hz according to the typical value of the Strouhal number St_d reported in the literature of about 0.0015 (Mi and Nathan 2004, 2006).

The bulk mean velocity V_j of the fluid entering the chamber is about 7.5 m/s, thus resulting in $Re_d = \frac{V_j d}{\nu} = 150,000$ where ν is the kinematic viscosity of water equal to about $10^{-6} \text{m}^2/\text{s}$. For these experimental conditions, the precessing mode is expected to be prevalent on the axial mode; indeed, Madej et al. (2011) indicated a probability of 65 % of precessing motion for $Re_d = 61,900$, $L/D = 2.75$ and $D/d = 5$; besides that, the probability weakly increases with Re_d .

It is known from previous works that the nature of the inlet flow has a significant influence on the probability of precession (Wong et al. 2004). According to Mi et al. (2001b, 2007), the inlet flow has also a significant influence on the shedding of structures embedded in the shear layer. The profiles of the axial velocity V/V_0 (being V_0 the maximum axial velocity) at the exit of the nozzle have been measured with stereo PIV (2D-3C PIV) for the case of outflow without the external chamber at $Re_d = 150,000$; the measurement has been conducted in order to characterize the inlet conditions along the XZ and XY directions (see Fig. 1 for the reference frame). A sequence of 1,000 instantaneous realizations has been captured with two PCO SensiCam cameras ($1,280 \times 1,024$ pixels, $6.67 \mu\text{m}$ pixel pitch), with a time delay equal to $80 \mu\text{s}$. A measurement domain of about $3d \times 2.1d$ is observed. The optical calibration is performed in the same way of the tomographic PIV test (see Sect. 2.3). The raw images are dewarped onto a common grid with a

Fig. 1 Details of the fluidic precessing nozzle with reference coordinate frame

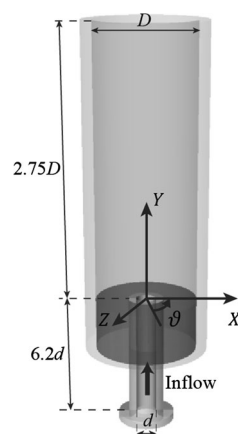


Fig. 2 Schematic representation of the illumination and imaging setup

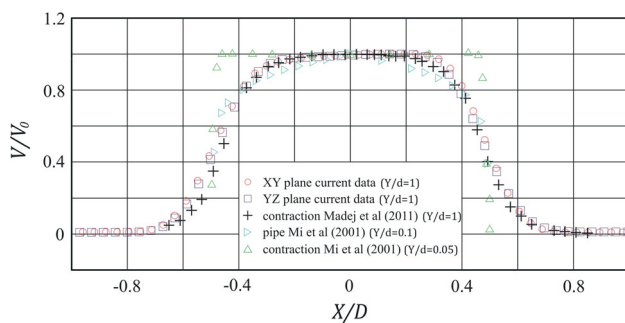
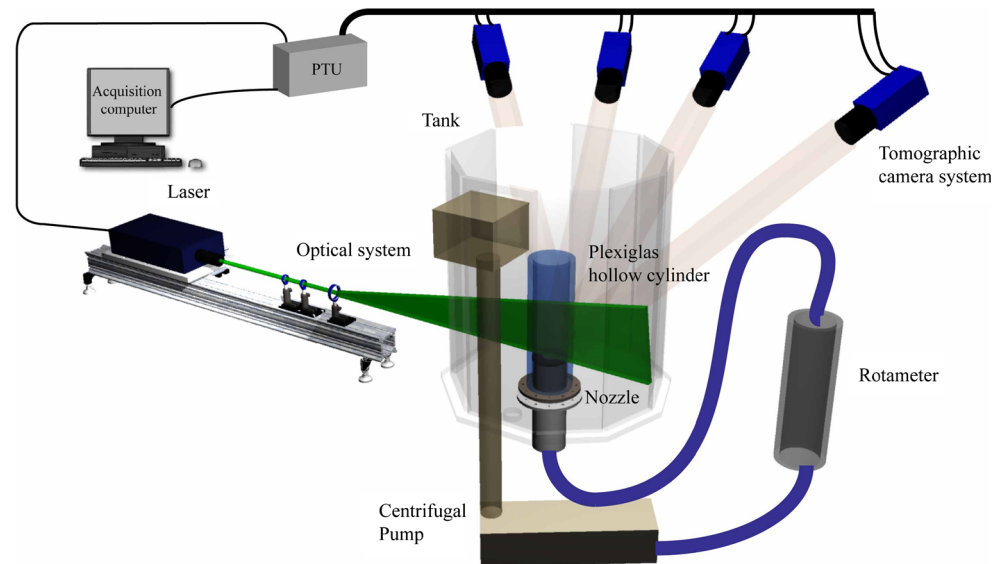


Fig. 3 Radial profiles of the mean axial velocity V normalized versus the jet centerline velocity V_0 for the current dataset along the XY (square box) and YZ (circle) planes compared with contoured (triangle, plus), pipe Mi et al. (2001b), Madej et al. (2011)

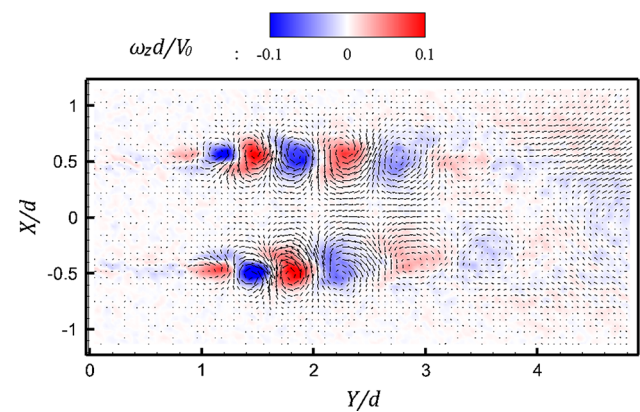


Fig. 4 Most energetic POD mode of the free jet flow issued by the nozzle at $Re_d = 16,000$. Velocity vectors plotted at each two measured vectors and contour plot of the $\omega_z d/V_0$

resolution of 16 pixels/mm. The image interrogation is performed with the adaptive method implemented by Astarita (2009), with window size of 64×64 pixels, 75 % overlap, and Blackman filtering within the interrogation process to tune the spatial resolution (Astarita 2007). The results reported in Fig. 3 versus previous literature data (Mi et al. 2001b; Madej et al. 2011) do not show any significant evidence of asymmetry and residual bias.

In order to further characterize the nozzle exit conditions, a planar PIV experiment has been conducted on the unconfined jet. The tested Reynolds number is reduced down to $Re_d = 16,000$ in order to improve the detectability of the vortical structures in the shear layer. In this case, a larger domain in the streamwise direction is taken into account, in order to characterize the streamwise evolution of the large coherent structures of the jet shear layer. As in the previous case, 1,000 realizations have been captured

with a time delay of 950 μ s. The area is discretized with 12 pixels/mm, corresponding to a measurement domain of about $4d \times 5d$. The method implemented by Discetti and Adrian (2012) is used to reduce the magnification measurement error. The application of POD (POD, see Sect. 2.3 for implementation details) allows the characterization of the shedding features within the shear layer of the unconfined jet. Figure 4 reports the most energetic POD mode, where the presence of axisymmetric ring-vortices is outlined from the contour representation of the normalized out-of-plane vorticity $\omega_z d/V_0$.

2.2 Tomographic PIV: procedure and data processing

An optical calibration is performed by recording images of a two levels calibration target (the separation between the

levels is 3 mm) mechanically translated along the depth direction of the measurement volume in the range ± 20 mm. The calibration markers are white dots on a dark background, with a regular spacing of 15 mm along two orthogonal directions. A template-matching technique, with a cross-correlation based algorithm, is used to identify the location of the markers. The root mean square (rms) of the initial calibration error is about 0.8 pixels.

The challenge in the application of this procedure resides in the practical difficulty to perform the calibration in situ due to physical restrictions, i.e., the calibration is performed without the presence of the chamber. For this reason, the volume self-calibration (Wieneke 2008) is used to correct the mapping functions to account for misalignment of the lines of sight due to refraction effects along the optical path (as done by Baum et al. 2013 and Ceglia et al. 2014). The final rms of the calibration error is reduced down to 0.05 pixels.

The acquisition and the pre-processing of the set of 500 images are performed using LaVision DaVis 8. Spatial-temporal sliding minimum with a kernel of 13×13 pixels in space and five images in time is subtracted from the images to reduce the background noise; local image intensity normalization is performed using the mean value of a $1,000 \times 1,000$ pixels kernel so that particle intensities are of similar magnitude for all the four cameras. A measurement volume of $100 \times 250 \times 34 \text{ mm}^3$ (i.e., $1D \times 2.5D \times 0.34D$) is reconstructed using a custom-made multiresolution algorithm with MLOS initialization, three MART iterations on a binned $2 \times$ configuration and two final MART iterations on the final resolution (Discetti and Astarita 2012a). A further accuracy improvement is obtained by applying the SFIT technique (Discetti et al. 2013) with anisotropic filtering on a $3 \times 3 \times 1$ kernel, with Gaussian distribution of weights and standard deviation equal to 1. The volume is discretized with 10 voxels/mm, thus resulting in a reconstruction volume of $1,000 \times 2,500 \times 340$ voxels.

The cross-correlation analysis is performed using an algorithm based on direct sparse cross-correlations and operations redundancy avoidance (Discetti and Astarita 2012b). The final interrogation spot is 64^3 voxels (corresponding to $6.4 \times 6.4 \times 6.4 \text{ mm}^3$) with 75 % overlap (thus resulting in a vector spacing of 1.6 mm). The uncertainty on the velocity measurement can be assessed by applying physical criteria, for example, by computing the divergence of the velocity field (Scarano and Poelma 2009). The uncertainty in the divergence is both due to the measurement error on the velocity and the numerical truncation in the derivatives calculation; however, the 75 % overlap reduces this second source of error, thus making it possible to quantify with reasonable approximation the uncertainty on the velocity measurement using the standard deviation of

the divergence. Considering the typical value of the vorticity within the shear layer (0.2 voxels/voxel) as a reference, for the raw velocity field, the standard deviation is 0.028 voxels/voxel (i.e., 14 % uncertainty); the uncertainty is reduced to 0.023 voxels/voxel (i.e., 11.5 % uncertainty) if a low-pass Gaussian filter on a kernel $3 \times 3 \times 3$ and standard deviation equal to 1 is applied.

2.3 Proper orthogonal decomposition implementation

The POD is a mathematical procedure that identifies an orthonormal basis using functions estimated as solutions of the integral eigenvalue problem known as Fredholm equation (see Sirovich 1987 for a rigorous formulation). Berkooz et al. (1993) have shown that the POD represents a powerful technique to extract relevant information about the coherent structures in turbulent flows. Consider a function (e.g., a velocity field) $\underline{U}(\underline{x}, t)$ that is approximated as:

$$\underline{U}(\underline{x}, t) = \langle \underline{U}(\underline{x}, t) \rangle + \underline{u}(\underline{x}, t) = \langle \underline{U}(\underline{x}, t) \rangle + \sum_{n=1}^{N_m} f_n(t) \underline{g}_n(\underline{x}) \quad (3)$$

where \underline{x} and t are the spatial and temporal coordinates, respectively; the angular brackets indicate the operation of ensemble averaging; underbars are used for vectors. The functions $\underline{g}_n(\underline{x})$ constitute the decomposition basis of the fluctuating velocity field $\underline{u}(\underline{x}, t)$; $f_n(t)$ are the time coefficients. The symbol N_m indicates the number of modes used to decompose the velocity field. The solution is not unique as it depends on the chosen basis functions $\underline{g}_n(\underline{x})$. The snapshots method proposed by Sirovich (1987) assumes that the POD modes are calculated as the eigenmodes of the two-point temporal correlation matrix \underline{R} :

$$\underline{R} \underline{g} = \lambda \underline{g} \quad (4)$$

where $R_{ij} = \langle \underline{u}(\underline{x}_i, t) \cdot \underline{u}(\underline{x}_j, t) \rangle$. Since \underline{R} is a non-negative Hermitian matrix, it has a complete set of non-negative eigenvalues, whose magnitude indicates the energy contribution of the respective eigenmodes.

Ben Chiekh et al. (2004) introduced a procedure to reconstruct the flow field in the case of shedding-dominated velocity fields. The technique, referred as LOR, is based on approximating the sum of Eq. (3) with only the first two modes, representing the shedding contribution:

$$\underline{U}(\underline{x}, t) = \langle \underline{U}(\underline{x}, t) \rangle + \underline{u}(\underline{x}, t) \approx \langle \underline{U}(\underline{x}, t) \rangle + a_1(\varphi) \underline{g}_1(\underline{x}) + a_2(\varphi) \underline{g}_2(\underline{x}) \quad (5)$$

The coefficients $a_1(\varphi)$ and $a_2(\varphi)$ are phase terms; they are related to the shedding phase angle (and, consequently, are not independent):

$$a_1(\varphi) = \sqrt{2\lambda_1} \sin(\varphi) \quad (6)$$

$$a_2(\varphi) = \sqrt{2\lambda_2} \cos(\varphi) \quad (7)$$

where λ_1 and λ_2 are the first two eigenvalues obtained by the POD. It can be demonstrated that the low-order representation corresponds to the basic Fourier component of the flow field ensemble with respect to the reconstructed phase (van Oudheusden et al. 2005).

3 Results and discussion

Here and in the following, unless otherwise stated, the letters U , V and W indicate the velocity components along the X , Y and Z directions, respectively. The corresponding lower case letters u , v , w refer to the components of the turbulent velocity fluctuations obtained by subtracting the mean velocity components from the instantaneous realizations. In the case of a cylindrical reference frame, V_r , V_θ and V (directed accordingly to Fig. 1) indicate the components along the radial, azimuthal and axial directions, respectively. Finally, the symbols u' , v' and w' are used to refer to the root mean square of the turbulent velocity fluctuations. The results are presented in non-dimensional form, using the bulk jet velocity V_j and the chamber diameter D as reference quantities.

3.1 Mean flow features of the precessing motion

The flow field switches intermittently between the axial and the precessing mode; flow visualizations on the present experimental apparatus have confirmed that the precession occurs in both directions, i.e., it can restart in opposite direction after having switched to the axial mode (Nathan et al. 1998). It means that the average flow field is not expected to have a net swirling component.

In order to identify the features of the precessing motion, the turbulent statistics are calculated by isolating the samples in which the jet precesses in the counter-clockwise direction using the phase-identifying method outlined in the following Sect. 3.2. The isolated samples need to respect the condition that at least for three consecutive realizations, they keep the same sign of the time derivative of the phase (i.e., the direction of precession stays unchanged). This condition ensures that at least for three realizations, the jet precesses in one direction.

The mean flow field obtained by averaging a set of 175 snapshots is illustrated in Fig. 5. The turbulent kinetic energy (TKE) contour plot in the $Z/D = 0$ and the iso-surfaces of both $\langle V \rangle / V_j = 0.99$ and of the swirl component of the velocity vector (namely $\langle V_\theta \rangle / V_j = 0.2$) are presented. A net nonzero swirl component is detected in

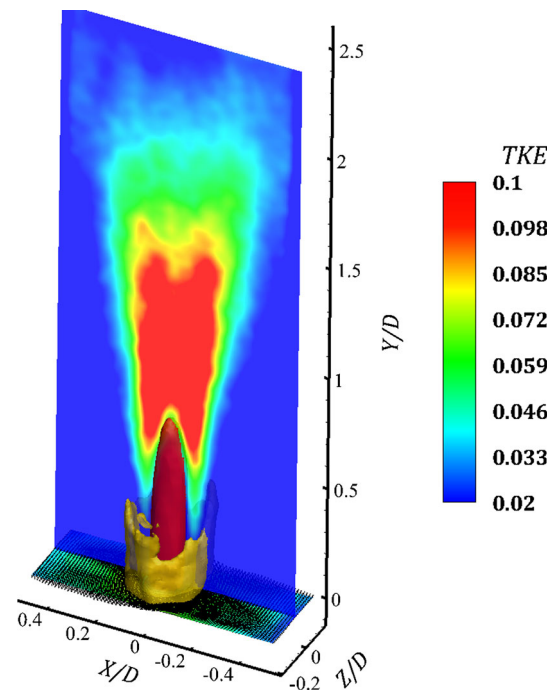


Fig. 5 Contour representation of the TKE on the middle plane of the measurement volume and of the azimuthal velocity on the nozzle exit section; iso-surfaces of $V/V_j = 0.99$ (red) and of $V_\theta/V_j = 0.2$ (light brown)

proximity of the nozzle. It arises in the jet shear layer in order to balance the overall angular momentum (i.e., in the opposite direction to that of the precession, in agreement with Dellenback et al. 1988); thus, its sign has an intimate bond with the precession direction.

Figures 6 and 7 represent the radial profiles of the mean velocity components and the rms of the turbulent fluctuations for three different streamwise locations ($Y/D = 0, 0.25$ and 0.5). The profiles of $\langle W \rangle / V_j$ confirm the presence of a significant swirl induced within the lower region of the chamber as already outlined in the description of the average field (Fig. 5). This effect is much stronger than the rate of entrainment of the jet in the near field, as testified by comparison with the profiles of $\langle U \rangle / V_j$, which are characterized by much weaker peaks. This difference is smeared out by diffusion when moving downstream (Fig. 6c), even though still clearly detectable.

At the nozzle exit, a significant intensity of the azimuthal fluctuations w'/V_j is observed, almost comparable to that of the axial fluctuations v'/V_j within the shear layer. By moving downstream, the latter remains dominant on the other two components. The gap between azimuthal (w'/V_j) and radial (u'/V_j) fluctuations decreases along the streamwise direction; it will be shown later (Sect. 3.3) that this effect can be addressed to the pairing of helical vortical structures formed within the shear layer due to local instabilities.

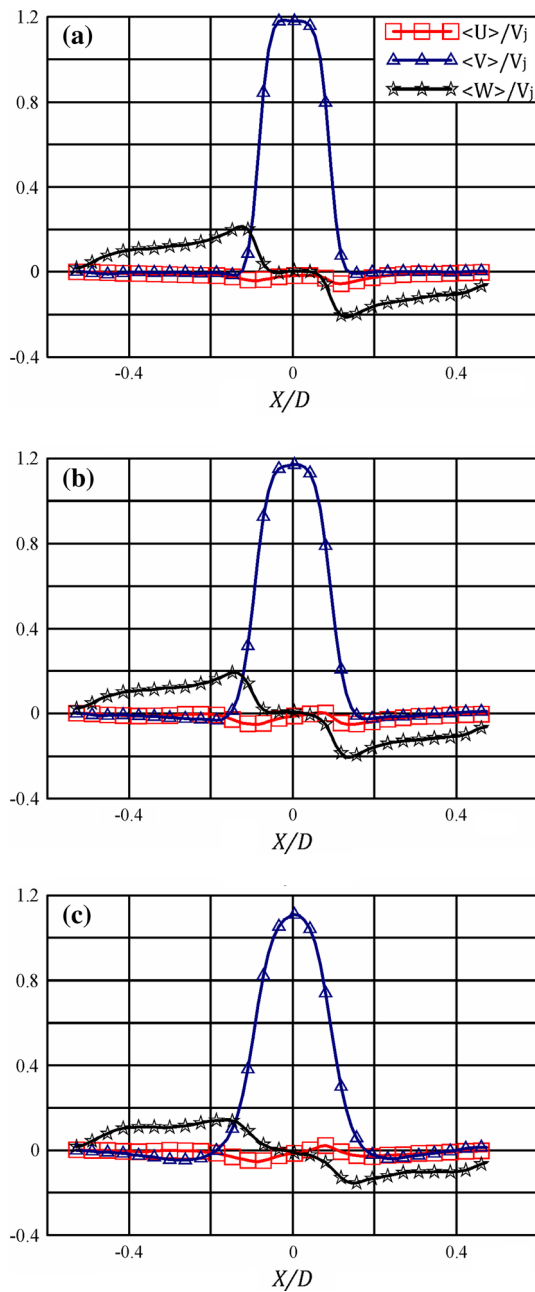


Fig. 6 Radial profiles of the mean velocity components for $Y/D = 0, 0.25, 0.5$ (top to bottom). Symbols are placed each three measured vectors

In order to characterize the degree of the induced swirl at the nozzle exit, the swirl number S is evaluated on the average flow field in the plane located at $Y/D = 0.01$ using the equation proposed in Toh et al. (2010):

$$S\left(\frac{r}{D}\right) = \frac{\int_0^r l^2 \langle V \rangle \langle V_\vartheta \rangle dl}{\int_0^r l \left(\langle V \rangle^2 - \frac{1}{2} \langle V_\vartheta \rangle^2 \right) dl} \quad (8)$$

where $\langle V_\vartheta \rangle$ and $\langle V \rangle$ are the mean azimuthal and axial velocity, respectively, and l is the abscissa along the radial

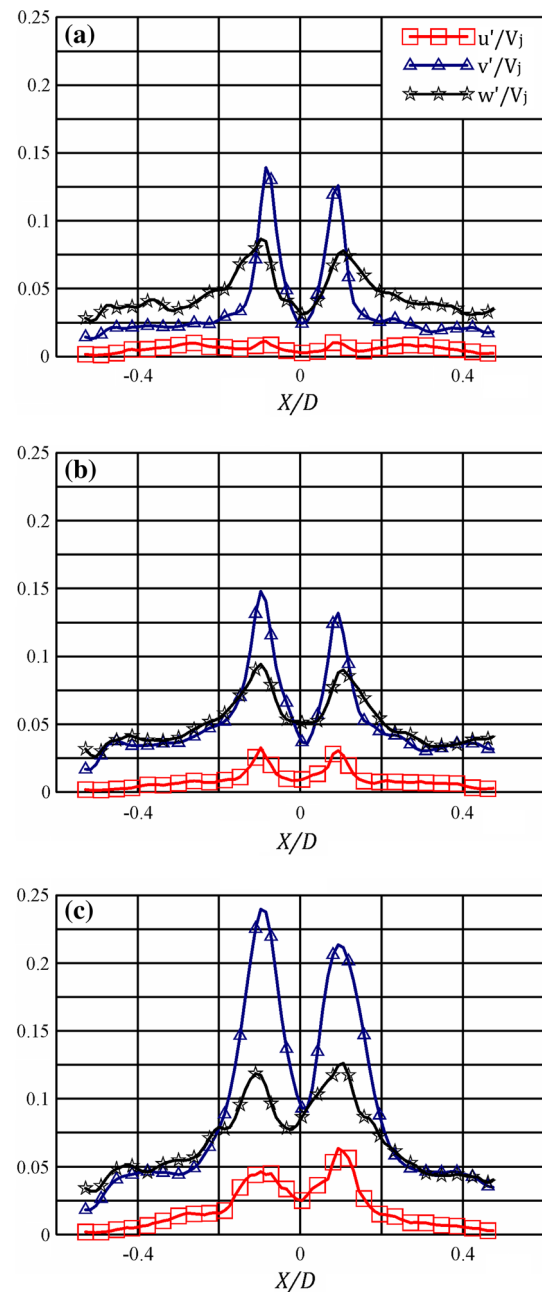


Fig. 7 Radial profiles of the rms of the normalized turbulent fluctuations for $Y/D = 0, 0.25, 0.5$ (top to bottom). Symbols are placed each three measured vectors

direction comprised between $0 \leq l \leq r/D$. The radial profile of the swirl number S is shown in Fig. 8. The maximum value $S = 0.04$ is reached at $r/D = 0.13$. This value is relatively small (swirling jets of industrial interest are typically characterized by $S > 0.6$, see for instance, Ceglia et al. 2014), but still significant considering that the inlet flow is swirl-free.

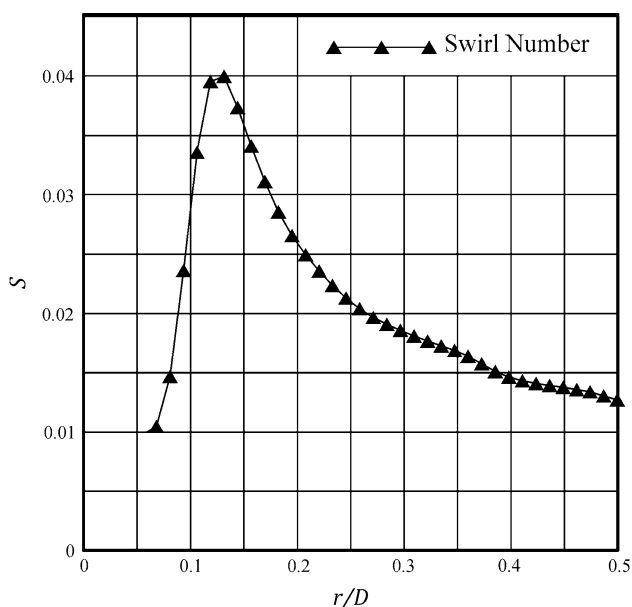


Fig. 8 Radial profile of the swirl number computed at axial station $Y/D = 0.01$

3.2 POD analysis and low-order reconstruction

The snapshots method (see Sect. 2.3) provides in principle a number of modes equal to the number of snapshots. For clarity, in Fig. 9a, the plot is limited only to the first 100 modes, containing about 70 % of the energy. The eigenvalues are normalized with respect to their sum, representing the total turbulent energy of the fluctuations. Furthermore, the cumulative sum of the energy is reported in Fig. 9b, in order to assess the number of modes that significantly contribute to build up the decomposition of the velocity field.

The first three modes are reported in Fig. 10, in which the contour representation on XZ slices of the v component normalized with the bulk velocity and the iso-surfaces of $v/V_j = \pm 0.15$ are reported. The first and second modes are associated with the large-scale precession, as they present

an asymmetric outflow associated with an inflow on the opposite side of the chamber. The difference in the energy pertaining to the first and to the second mode (20.8 and 10.9 %, respectively, see Fig. 9a) is probably related to the geometry of the measurement volume, since it contains the entire inflow and outflow regions for the case of the first mode, while in the second mode, the same two highly energetic regions are partly located outside of the observed volume in the far field. The third mode (with 7.5 % of energy) is practically axisymmetric, as it presents a strong on-axis outflow, and it can be associated with the axial mode. The ratio of the energy pertaining to the first two modes and the total energy of the first three modes can be interpreted as an “effective energy–probability” of precessing motion (leading to about 81 %). This result is practically in agreement with the measurements of Madej et al. (2011), which indicates 65 % precession probability at $Re_d = 61,900$ (monotonically increasing with Re_d) under the same geometrical conditions. It has to be noted, however, that the computation of the precession probability is affected by the uncertainty in the measure of the modal energy of the second mode.

As already reported in Sect. 2.3, when the bulk of the energy pertains only to few modes, the main features of the flow field can be highlighted using a LOR approach. In this case, only the first two modes are taken into account to describe the dynamics of the precessing motion. Equations (6, 7) can be rearranged as follow:

$$\sin(\varphi) = \frac{a_1(\varphi)}{\sqrt{2\lambda_1}} \tag{9}$$

$$\cos(\varphi) = \frac{a_2(\varphi)}{\sqrt{2\lambda_2}} \tag{10}$$

Equations (9–10) describe a circle in the normalized plane $\frac{a_1(\varphi)}{\sqrt{2\lambda_1}}, \frac{a_2(\varphi)}{\sqrt{2\lambda_2}}$ that would be associated with a pure shedding phenomenon (in this case the large-scale precession). The scatter plot of the time coefficients of the first two modes in this normalized plane is presented in Fig. 11. As stated before, there is an intermittent switch

Fig. 9 Energy distribution of the first 100 POD modes: **a** normalized eigenmodes; **b** cumulative energy

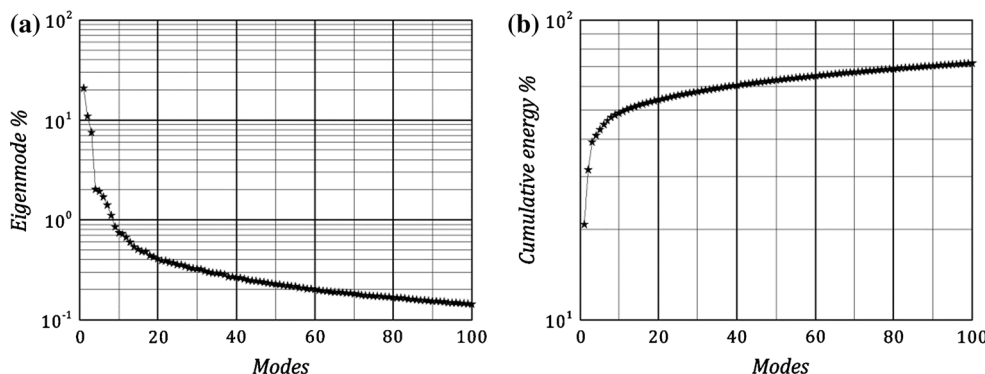


Fig. 10 Contour representation on XZ slices of the v/V_j , and iso-surfaces of $v/V_j = -0.15$ (blue) and $v/V_j = 0.15$ (red) for the first (a), second (b) and third (c) POD modes

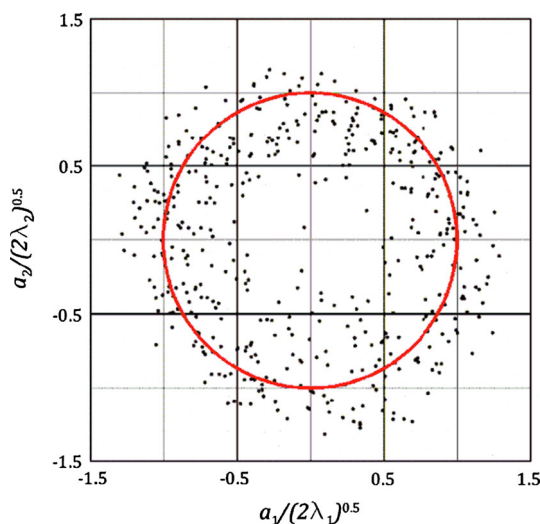
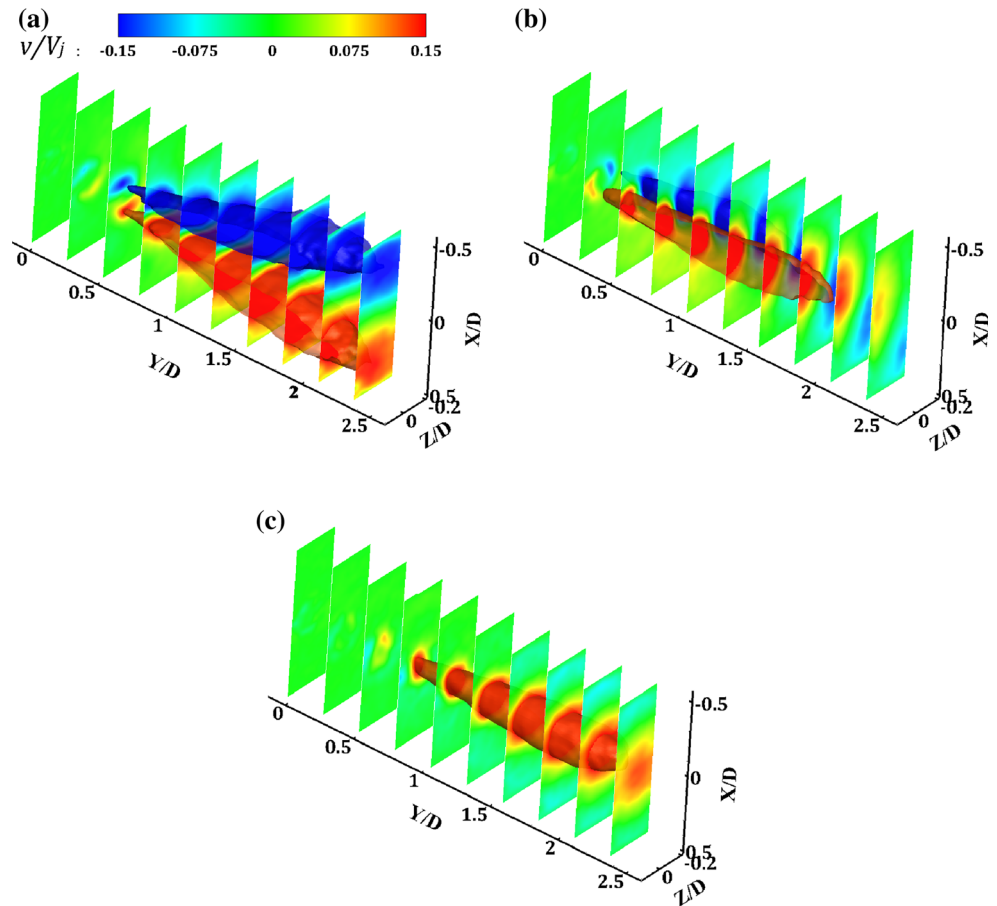


Fig. 11 Scatter plot of the time coefficients for the first two modes in the normalized plane. The circumference with radius 1 is plotted as a reference

between the precessing and axial motion; thus, the points are distributed all over the normalized plane. In order to isolate only those points pertaining to the precession, the

samples with $\frac{|a_3|}{\sqrt{2\lambda_3}} > 0.8$ and $\frac{|a_1|}{\sqrt{2\lambda_1}}, \frac{|a_2|}{\sqrt{2\lambda_2}} < 0.3$ have been excluded from the scatter plot. The samples isolated with this procedure, i.e., the points on the normalized plane that are most likely representative of jet flowing in the axial mode, are about 8 % of the entire set. The uncertainty in fixing the threshold for a_1 and a_2 and in determining the energy that pertains to the second mode explains the error in determining the precession probability with this method.

The flow fields obtained with the LOR are reported in Fig. 12 for $\varphi = 0^\circ, 90^\circ, 180^\circ, 270^\circ$. Since the present data set consists of 500 images acquired at 10 Hz (i.e., the observation time corresponds to only 50 s), one direction of precessing motion was strongly prevalent. As a result, the computed LOR is representative of this motion. The contour representation on the XZ slice is blanked if $V/V_j < 0.015$, thus highlighting only the outflow regions. The zones with stronger reverse flow are identified in blue with the iso-surfaces $V/V_j = -0.05$. The flow field topology, as expected, reveals the presence of a strongly asymmetric entrainment area located on the opposite side to that of the outflow in the far field of the chamber. This region is coupled with an extended recirculation zone (characterized by weaker negative velocity with respect to

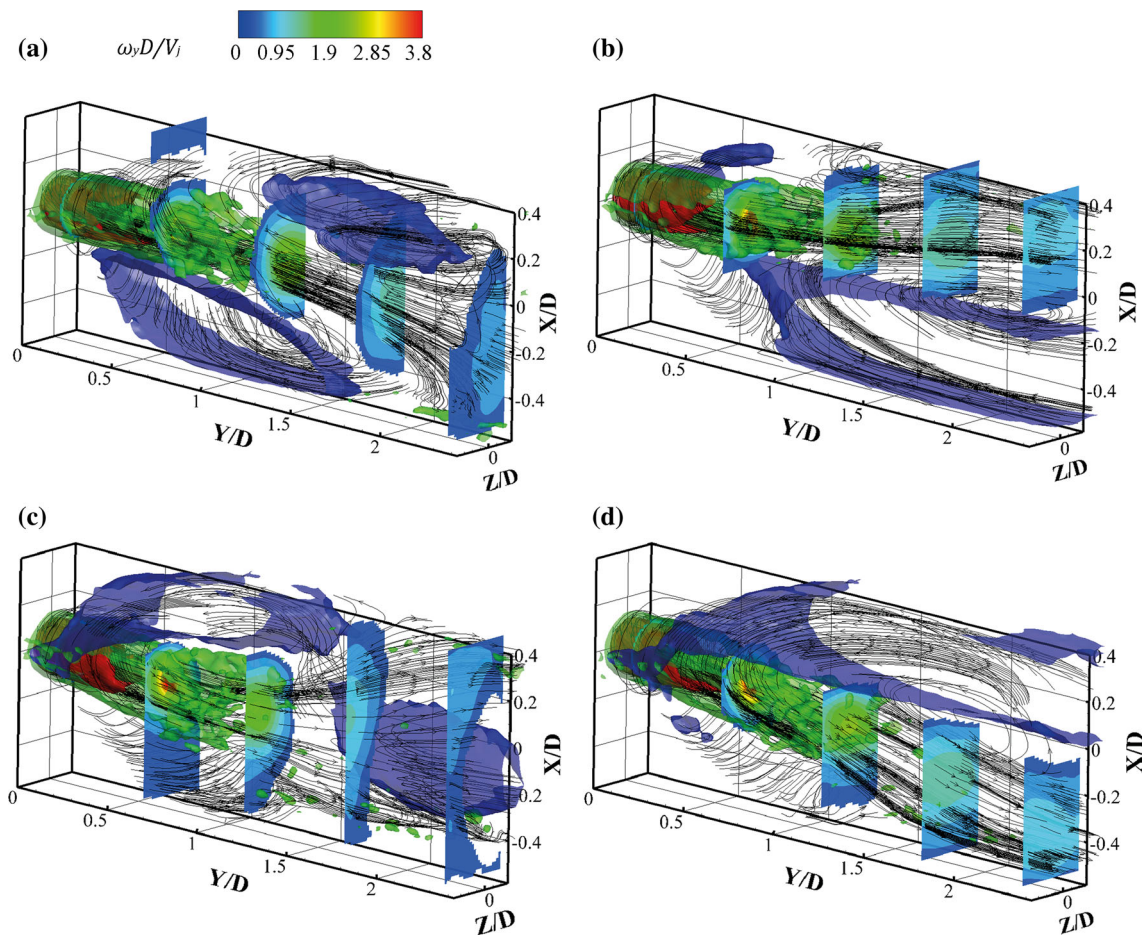


Fig. 12 Representation of the phase-resolved flow fields by means of LOR: **a** $\varphi = 0^\circ$, **b** $\varphi = 90^\circ$, **c** $\varphi = 180^\circ$, **d** $\varphi = 270^\circ$. Iso-surfaces of $V/V_j = -0.05$ (blue), $(\omega_y D)/V_j = 3.8$ (red), $(\omega_y D)/V_j = 0.8$ (green).

Contour representation of V/V_j on XZ planes (coloring blanked for $V/V_j = -0.05$)

the main entrainment one) located below the position of attachment of the exiting jet. The two recirculation regions asymmetrically embrace the jet attached to the wall and precess around it (see movie1); this determines a strong swirl arising in the near field, testified by the iso-surfaces of the Y -component of the normalized vorticity $(\omega_y D)/V_j$.

3.2.1 Precession frequency measurement

The phase of a single realization with respect to the precessing motion can be extracted using its time coefficients for the first two modes, i.e.,

$$\varphi = \arctan\left(\frac{\sqrt{2\lambda_2} a_1}{\sqrt{2\lambda_1} a_2}\right) \tag{11}$$

Equation (11) is applied on each sample to determine its phase; then the sequences are analyzed to identify patterns of regularly spaced phase angles. The results reported in Fig. 13 highlight a regular tendency of the jet to precess with a negative angular velocity, i.e., angular

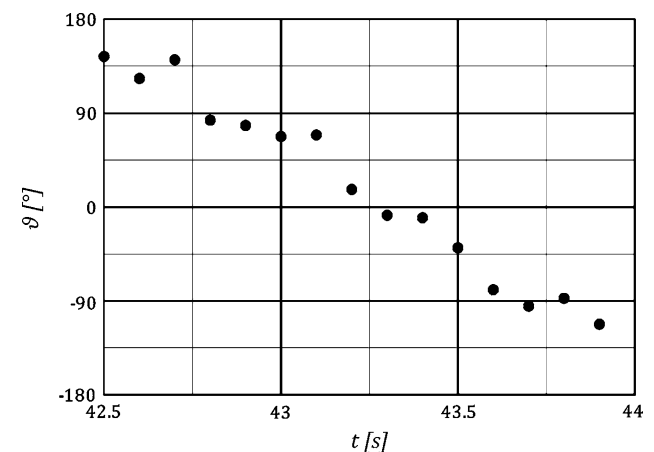


Fig. 13 Phase angles for a 1.5-s time interval

rate vector along the negative Y axis direction. This result confirms the intuition that the upstream swirl generated in the near field (and in particular in the jet

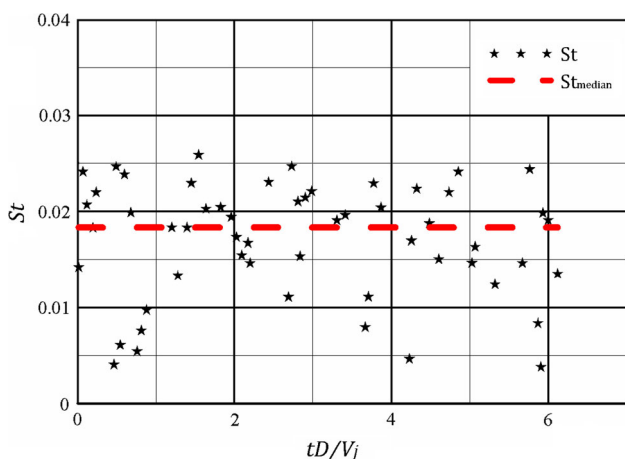


Fig. 14 Strouhal number distribution on the data set and relative median value

shear layer) is in the opposite direction to that of precession.

Sequences of samples with regularly spaced phases can be extracted to identify cycles of precession and provide a measurement of the Strouhal number (Fig. 14). The dispersion of the Strouhal number is addressed to the intermittency of the phenomenon and the uncertainty in determining the exact phase shift in the sequence analysis. The median of the Strouhal number distribution over the complete data set is about 0.0015 (corresponding to a precession frequency of 0.6 Hz), in agreement with the data reported in the literature (Mi and Nathan 2004, 2006).

3.3 Instantaneous flow field features and stability of the near field

An instantaneous realization of the velocity field for the tested nozzle is shown in Fig. 15. The normalized longitudinal velocity component V/V_j is presented with contour representations at six streamwise locations: $Y/D = 0$ and five regularly spaced slices between $Y/D = 0.25$ and $Y/D = 2.25$; iso-surfaces of $V/V_j = 0.4$, $V/V_j = -0.1$ and $QD^2/V_j^2 = 6$ (Jeong and Hussain 1995) are also reported.

The jet asymmetrically attaches to the wall and a wide entrainment region arises on the opposite side to that of impingement. The point of attachment is close to $Y/D = 2$ (thus at about 73 % of the chamber), in contrast with the surface visualization reported by Nathan et al. (1998), locating the impingement point about at half height of the chamber. Such a discrepancy is addressed to the presence of the exit lip in their experimental setup, which exasperates the exit angle (and, accordingly, the swirl number at the outlet of the chamber). Consequently, the attachment

point tends to move upstream due to the stronger induced swirl.

An azimuthal velocity component arises in correspondence with the nozzle exit section due to the jet precession and to the asymmetric recirculation region. This is evident looking at the mean flow field in Fig. 5. The Rayleigh stability criterion, presented in dimensionless form, for an inviscid swirling flow states that a necessary condition for the flow instability is (Drazin 2002):

$$K\left(\frac{r}{D}, \frac{Y}{D}\right) = \frac{1}{V_j^2 D} \frac{\partial}{\partial r} \left[V_\theta^2 \left(\frac{r}{D}, \frac{Y}{D}\right) r^2 \right] < 0 \tag{12}$$

Figure 16 shows that near the nozzle exit ($Y/D = 0.1$) the instability condition reported in Eq. (12) is satisfied for $r/D > 0.13$. The instability generates two helical vortices in the near field (Fig. 15, insert, and Fig. 17). The absence of the typical ring-vortex phenomenology of circular jets is due to the swirling motion induced by the jet precession. In Fig. 17, the qualitative path of the two helical structures is highlighted with dashed lines. Moving farther from the nozzle exit, these structures tend to merge losing coherence at approximately $Y/D = 0.5$, similarly to the pairing of ring vortices for a free jet (Winant and Browand 1974; Yule 1978). In correspondence with the pairing of the helical structures, the TKE assumes the maximum value, as it can be inferred from the average field in Fig. 5.

It can be concluded that for the present jet, i.e., in case of a jet issuing from a short pipe, the near field is characterized by the swirling motion that suppresses the generation of axisymmetric ring vortices and promotes the formation of azimuthal helical structures.

4 Conclusions

This work presents a tomographic PIV study of a PJ at $Re_d = 150,000$ issued from a short pipe in a coaxial cylindrical chamber with an expansion ratio equal to 5:1 and a length of 2.75 chamber diameters.

The present measurements confirm that the driving force of the precession is the inertial effect induced by the asymmetric entrainment on the opposite side of that of the outflow (Nathan et al. 1998). The entrainment region is extended along the chamber and interacts with an asymmetric recirculation zone, placed right below the exiting jet and extending down to the basis of the chamber.

The POD is used to analyze the energetic contribution of the precessing and the axial modes. The first two modes contain the bulk of the energy associated with the precession, while the third mode is representative of the axial mode. The ratio of the energy associated with the precessing modes and the axial one is used to infer the

Fig. 15 Contour representation of the instantaneous longitudinal velocity component V/V_j on XZ planes of the measurement volume and iso-surfaces of $V/V_j = 0.4$ (red), $V/V_j = -0.1$ (blue) and $QD^2/V_j^2 = 6$ (green). A magnified view of the vortical structures in the near field is reported in the insert. Flow is from right to left

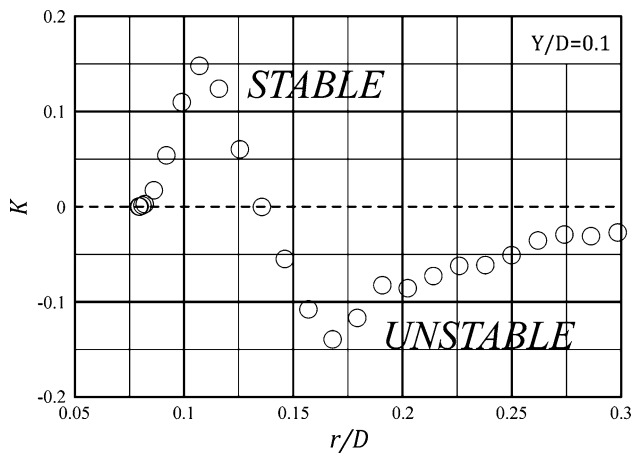
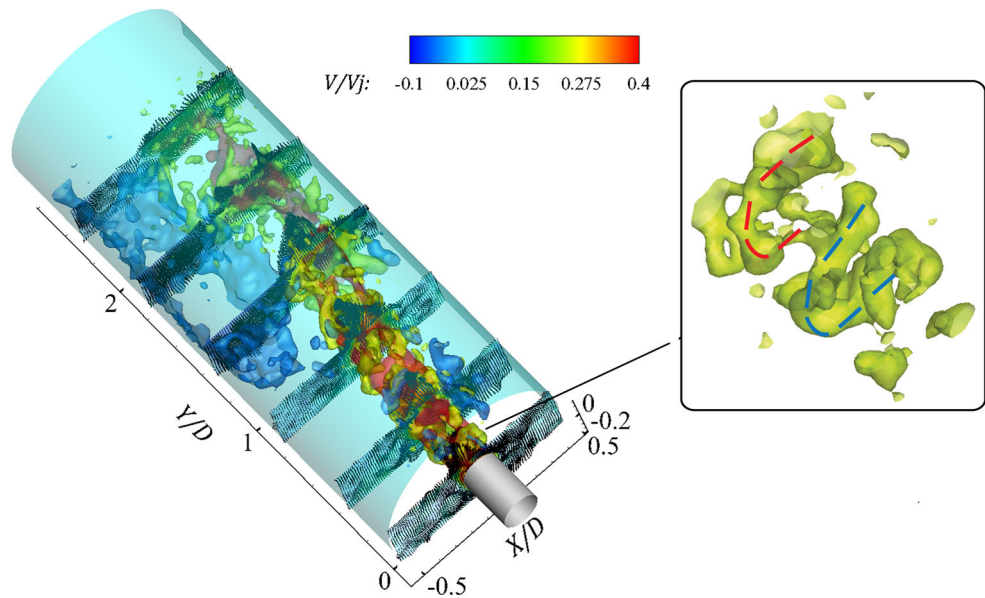


Fig. 16 Radial distribution of the Rayleigh stability criterion coefficient ($Y/D = 0.1$)

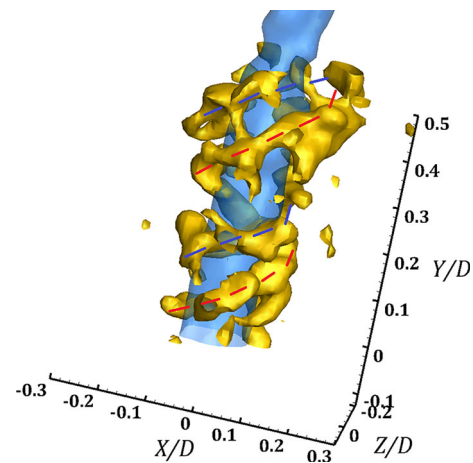


Fig. 17 Helical structures identification (red and blue dashed lines) on an instantaneous realization. Iso-surface for $V/V_j = 0.99$ (light blue). Vortical structures are identified using the Q criterion (yellow iso-surface, $QD^2/V_j^2 = 6$)

precession probability. Even though the present data are affected by a residual uncertainty due to the shape of the measurement volume, the result is in good agreement with the values foreseen at the tested Re_d from the literature data (Madej et al. 2011).

A LOR of the precessing motion highlights the dynamics of the interaction between the entrainment of external (to the chamber) fluid and the recirculation region in the lower part of the chamber. This interaction is responsible for the rising of a swirling motion into the shear layer of the jet in the direction opposite to that of precession to balance the overall angular momentum (Dellenback et al. 1988).

The induced swirling flow results to be unstable and generates two helical vortices. These structures evolve

along the streamwise direction for about $5d$ where the coherence of the structure ceases and the vortices merge according to the pairing phenomenon. Surprisingly enough, the formation of vortex rings due to the Kelvin–Helmholtz instability (visualized in free jet conditions) does not occur, as it is replaced by the helical vortices. This leads to the conclusion that the PJ issued from a short pipe behaves much more like a swirling jet than a round jet also in the near field.

Acknowledgments The authors kindly acknowledge LaVision GmbH for providing the cameras used in the experiments.

References

- Adrian RJ, Westerweel J (2011) Particle image velocimetry. Cambridge University Press, Cambridge
- Astarita T (2007) Analysis of weighting windows for image deformation methods in PIV. *Exp Fluids* 43:859–872
- Astarita T (2009) Adaptive space resolution for PIV. *Exp Fluids* 46:1115–1123
- Baum E, Peterson B, Surmann C, Michaelis D, Böhm C, Dreizler A (2013) Investigation of the 3D flow field in an IC engine using tomographic PIV. *Proc Combust Inst* 34:2903–2910
- Ben Chiekh M, Michard M, Grosjean N, Bera JC (2004) Reconstruction temporelle d'un champ aérodynamique instationnaire à partir de mesures PIV non résolues dans les temps. 9^e Congrès Francophone de Vélocimétrie Laser, Bruxelles, Belgium
- Berkooz G, Holmes P, Lumley JL (1993) The proper orthogonal decomposition in the analysis of turbulent flows. *Annu Rev Fluid Mech* 25:539–575
- Broadwell JE, Mungal MG (1991) Large-scale structures and molecular mixing. *Physics Fluids A*3:1193–1206
- Buckingham E (1914) On physically similar systems: illustration of the use of dimensional equations. *Physically Similar Systems*. *Phys Rev* 4:345–376
- Ceglia G, Discetti S, Ianiro A, Michaelis D, Astarita T, Cardone G (2014) Three-dimensional organization of the flow structure in a non-reactive model aero engine lean burn injection system. *Exp Therm Fluid Sci* 52:164–173
- Dellenback PA, Metzger DE, Neitzel GP (1988) Measurements in turbulent swirling flow through an abrupt axisymmetric expansion. *AIAA J* 26:669–681
- Discetti S, Adrian RJ (2012) High accuracy measurement of magnification for monocular PIV. *Measurement Sci Technol* 23:117001
- Discetti S, Astarita T (2012a) A fast multi-resolution approach to tomographic PIV. *Exp Fluids* 52:765–777
- Discetti S, Astarita T (2012b) Fast 3D PIV with direct sparse cross-correlations. *Exp Fluids* 53:1437–1451
- Discetti S, Natale A, Astarita T (2013) Spatial filtering improved tomographic PIV. *Exp Fluids* 54:1505–1517
- Drazin PG (2002) Introduction to hydrodynamic stability. Cambridge texts in Applied Mathematics
- Guo B, Langrish TAG, Fletcher DF (2001) Numerical simulation of unsteady turbulent flow in axisymmetric sudden expansions. *J Fluids Eng* 123:574–587
- Jeong J, Hussain F (1995) On the identification of a vortex. *J Fluid Mech* 285:69–94
- Madej AM, Babazadeh H, Nobes DS (2011) The effect of chamber length and Reynolds number on jet precession. *Exp Fluids* 51:1623–2643
- Mi J, Nathan GJ (2004) Self-excited jet-precession Strouhal number and its influence on downstream mixing field. *J Fluids Struct* 19:851–862
- Mi J, Nathan GJ (2006) The effect of inlet flow condition on the frequency of self-excited jet precession. *J Fluids Struct* 22:129–133
- Mi J, Nathan GJ, Luxton RE (2001a) Mixing characteristics of a flapping jet from a self-exciting nozzle. *Flow Turbul Combust* 67:1–23
- Mi J, Nathan GJ, Nobes DS (2001b) Mixing characteristics of axisymmetric free jets from a contoured nozzle, an orifice plate and a pipe. *J Fluids Eng* 123(4):878–883
- Mi J, Kalt PAM, Nathan GJ, Wong CY (2007) PIV measurements of turbulent jet issuing from a round sharp-edged plate. *Exp Fluids* 42:625–637
- Nathan GJ, Luxton RE, Smart JP (1992) Reduced NO_x emissions and enhanced large scale turbulence from a precessing jet burner. *Symp (Int) Combust* 24:1399–1405
- Nathan GJ, Hill SJ, Luxton RE (1998) An axisymmetric 'fluidic' nozzle to generate jet precession. *J Fluid Mech* 370:347–380
- Nathan GJ, Mi J, Alwahabi ZT, Newbold GJR, Nobes DS (2006) Impacts of a jet's exit flow pattern on mixing combustion performance. *Prog Energy Combust Sci* 32:469–538
- Newbold GJR, Nathan GJ, Nobes DS, Turns SR (2000) Measurement and prediction of NO_x emissions from unconfined propane flames from turbulent jet, bluff body, swirl and precessing jet burners. *Symp (Int) Combust* 28:481–487
- Revuelta A, Sánchez AL, Liñán A (2004) Confined swirling jets with large expansion ratios. *J Fluid Mech* 508:89–98
- Reynolds WC, Parekh DE, Juvet PJD, Lee MJD (2003) Bifurcating and blooming jets. *Ann Rev Fluid Mech* 35:295–315
- Scarano F (2013) Tomographic PIV: principles and practice. *Measurement Sci Technol* 24:012001
- Scarano F, Poelma C (2009) Three-dimensional vorticity patterns of cylinder wakes. *Exp Fluids* 47:69–83
- Simmons JM, Platzer MF, Lai JCS (1981) Jet excitation by an oscillating vane. *AIAA J* 19:673–676
- Sirovich L (1987) Turbulence and the dynamics of coherent structures. *Q Appl Math* 45:561–590
- Stamatov V, Stamatova L (2006) A Mie scattering investigation of the effect of strain rate on soot formation in precessing jet flames. *Flow Turbul Combust* 76:279–289
- Syred N (2006) A review of oscillation mechanisms and the role of the precessing vortex core (PVC) in swirl combustion systems. *Prog Energy Combust Sci* 32:93–161
- Toh K, Honnery D, Soria J (2010) Axial plus tangential entry swirling jet. *Exp Fluids* 48:309–325
- van Oudheusden BW, Scarano F, van Hinsberg NP, Watt DW (2005) Phase-resolved characterization of vortex shedding in the near wake of a square section cylinder at incidence. *Exp Fluids* 39:86–98
- Violato D, Ianiro A, Cardone G, Scarano F (2012) Three-dimensional vortex dynamics and convective heat transfer in circular and chevron impinging jets. *Int J Heat Fluid Flow* 37:22–36
- Wieneke B (2008) Volume self-calibration for 3D particle image velocimetry. *Exp Fluids* 45:549–556
- Winant CD, Browand FK (1974) Vortex pairing: the mechanism of turbulent mixing-layer growth at moderate Reynolds number. *J Fluid Mech* 63:237–255
- Wong CY, Lanspeary PV, Nathan GJ, Kelso RM, O'Doherty T (2003) Phase averaged velocity in a fluidic precessing jet nozzle and its near external field. *Exp Thermal Fluid Sci* 27:515–524
- Wong CY, Nathan GJ, O'Doherty T (2004) The effect of initial conditions on the exit flow from a fluidic precessing jet nozzle. *Exp Fluids* 36:70–81
- Yule AJ (1978) Large-scale structure in the mixing layer of a round jet. *J Fluid Mech* 89:413–432